nature astronomy

Article

https://doi.org/10.1038/s41550-024-02347-z

The interior as the dominant water reservoir in super-Earths and sub-Neptunes

Received: 17 August 2023

Accepted: 23 July 2024

Published online: 20 August 2024

Check for updates

Haiyang Luo ^{1,3} ∠, Caroline Dorn ^{2,3} ∠ & Jie Deng ¹ ∠

Water is an important component of exoplanets, with its distribution, that is, whether at the surface or deep inside, fundamentally influencing the planetary properties. The distribution of water in most exoplanets is determined by yet-unknown partition coefficients at extreme conditions. Here we first conduct ab initio molecular dynamics simulations to investigate the metal-silicate partition coefficients of water up to 1,000 GPa and then model planet interiors by considering the effects of water content on density, melting temperature and water partitioning. Our calculations reveal that water strongly partitions into iron over silicate at high pressures and, thus, would preferentially stay in a planet's core. The results of our planet interior model challenge the notion of water worlds as imagined before: the majority of the bulk water budget (even more than 95%) can be stored deep within the core and the mantle, and not at the surface. For planets more massive than ~6 M_{\oplus} and Earth-size planets (of lower mass and small water budgets), the majority of water resides deep in the cores of planets. Whether water is assumed to be at the surface or at depth can affect the radius up to 15-25% for a given mass. The exoplanets previously believed to be water-poor on the basis of mass-radius data may actually be rich in water.

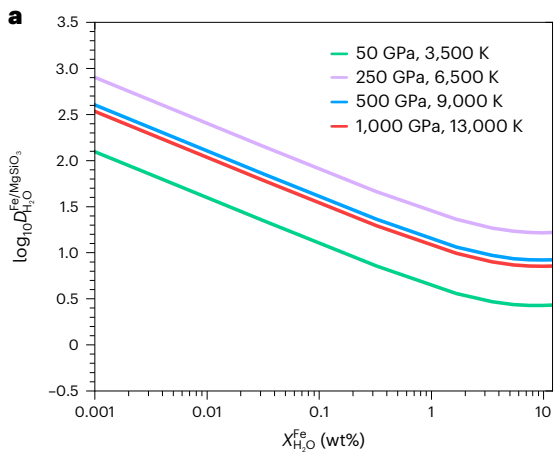
The majority of detected super-Earths and sub-Neptunes are expected to have been hosting global magma oceans since formation, due to their high initial temperatures and limited cooling resulting from intense irradiation from host stars. Magma oceans serve as crucial reservoirs for storing volatiles, particularly water, which exhibits higher solubility compared with other gas species¹. Hence, water can be present deep within planetary interiors². Additionally, water-rich worlds are predicted by planet formation theories³, further supporting the abundance of water. While the dissolution of volatiles has been considered in recent years in theoretical studies on interior modelling⁴⁻⁶, the majority of present-day interior models used for interpreting exoplanet mass-radius data commonly assume that all water exists solely at the surface of a rocky interior, neglecting the presence of water deep within planetary interiors. Efforts to reach high accuracy in observed massradius data must be matched with precise theoretical interior models. This involves developing a comprehensive and realistic description of

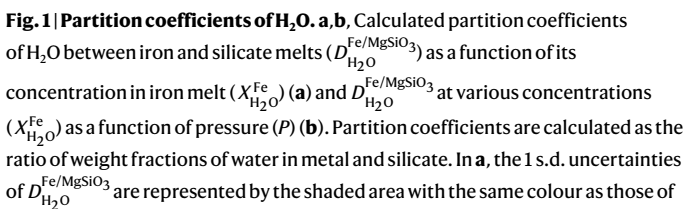
how different planet building materials, such as iron, silicate, water and gas, interact.

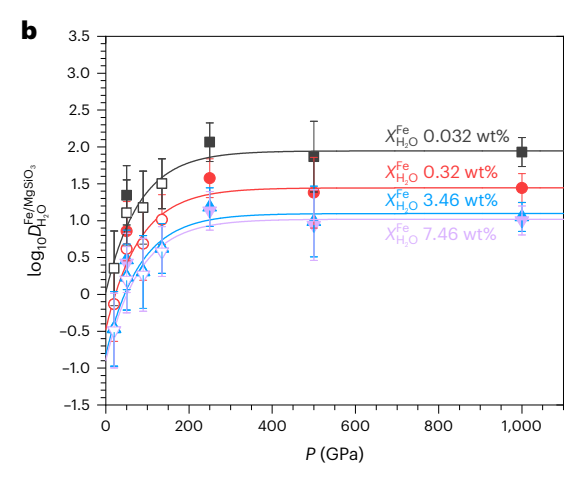
Here, we focus on water partitioning between an iron core, a silicate mantle and a surface reservoir. The water partitioning behaviour between silicate melt and vapour has been well established⁷. Notably, a previous study suggests that hidden water in magma oceans may result in a deviation in planet radius of up to 16% given a fixed planet mass and bulk composition⁸. No studies have yet explored the water partitioning between iron and silicate melt under the extreme pressure and temperature conditions relevant to super-Earths and sub-Neptunes. Water in the metallic core is especially important because these waters will be locked away for the lifetime of the planet, while water in the mantle can be outgassed over time (Supplementary Discussion). Taking Earth as an essential reference point for studying rocky exoplanets, recent studies indicate a strong influence of Earth's core on the distribution of water and suggest that 37-73 Earth ocean

Department of Geosciences, Princeton University, Princeton, NJ, USA. 2Institute for Particle Physics and Astrophysics, ETH Zurich, Zurich, Switzerland.

³These authors contributed equally: Haiyang Luo, Caroline Dorn. 🖂 e-mail: haiyang.luo@princeton.edu; dornc@ethz.ch; jie.deng@princeton.edu







the respective lines. In \mathbf{b} , the open symbols are previous computational data°. The solid symbols represent our results. The error bars represent 1 s.d. uncertainties of $D_{\mathrm{H}_2\mathrm{O}}^{\mathrm{Fe/MgSiO}_3}$. Using the 32 data points shown, $D_{\mathrm{H}_2\mathrm{O}}^{\mathrm{Fe/MgSiO}_3}$ is parametrized as a function of H₂O concentration in iron melt, $X_{\mathrm{H}_2\mathrm{O}}^{\mathrm{Fe}}$ (in wt%) and P (in GPa) with the equation $\log_{10}D_{\mathrm{H}_2\mathrm{O}}^{\mathrm{Fe/MgSiO}_3} = 1.26 - 0.34 \log_{10}X_{\mathrm{H}_2\mathrm{O}}^{\mathrm{Fe}} + 0.08 \left(\log_{10}X_{\mathrm{H}_2\mathrm{O}}^{\mathrm{Fe}}\right)^2 - 4,007/\left(1 + \exp\left(\left(\frac{P + 616}{80.6}\right)\right)\right)$.

masses of water are stored in the core as water has large metal–silicate partition coefficients ($D_{\rm H_2O}^{\rm metal/silicate}$ = water mass fraction in metal/water mass fraction in silicate \geq 29) at core formation conditions (up to ~135 GPa and 4,200 K) $^{9-11}$. Super-Earths and sub-Neptunes with larger masses and surface gravities experience higher pressures (up to ~1,400 GPa) and temperatures (up to ~14,000 K) during their core formation. Without the data obtained at the relevant P/T conditions, it is difficult to estimate the metal–silicate partitioning behaviour of water at the conditions of super-Earths and sub-Neptunes, given the ~10 times larger pressures and the induced drastic structural changes of metal and silicate. In fact, extrapolated values 9,11 of $D_{\rm H_2O}$ at these conditions remain inconsistent with each other and span a wide range from 0 to 10^{11} (Supplementary Fig. 1), rendering the water distribution in super-Earths and sub-Neptunes largely unconstrained.

In this study, we calculate partition coefficients of H₂O between iron and silicate melt ($D_{\rm H_2O}^{\rm Fe/MgSiO_3}$) using ab initio molecular dynamics simulations coupled with the thermodynamic integration (TI) technique (Methods). This method has been successfully applied to predict the metal-silicate partitioning of many elements, including hydrogen⁹, boron¹² and noble gases^{13,14}. We first test our calculations at 50 GPa/3,500 K and find that our results are in good agreement with a previous study (Fig. 1). We then initiate our calculations at three hypothetical conditions for super-Earths: 250 GPa/6,500 K, 500 GPa/9.000 K and 1.000 GPa/13.000 K (Extended Data Fig. 1 and Extended Data Table 1). The assumed temperatures are near the estimated silicate liquidus and iron melting points at these pressures and guarantee the liquid state of our simulations. We then investigate the temperature dependence of H₂O partitioning based on the Gibbs-Helmholtz equation by calculating enthalpies at various temperatures at fixed pressures (Extended Data Figs. 2 and 3 and Extended Data Table 2). In addition to the TI method, we also perform direct two-phase molecular dynamics simulations of metal-silicate co-existence to gain further insight into the lithophile or siderophile nature of water (Extended Data Fig. 4).

Our results based on the TI method reveal that, under the extreme conditions of super-Earths and sub-Neptunes, $\rm H_2O$ remains siderophile and exhibits comparable partition coefficients $D_{\rm H_2O}^{\rm Fe/MgSiO_3}$ at 250 GPa/6,500 K, 500 GPa/9,000 K and 1,000 GPa/13,000 K within

error (Fig. 1a). $D_{\rm H_2O}^{\rm Fe/MgSiO_3}$ decreases with concentration of H₂O in iron melt ($X_{\rm H_2O}^{\rm Fe}$) and plateaus when $X_{\rm H_2O}^{\rm Fe}$ exceeds around 7 wt%. This is because more H₂O tends to enter iron melt to maximize the mixing entropy when the concentration of H₂O in iron melt is low, and this effect on entropy decreases with increasing $X_{\rm H_2O}^{\rm Fe}$. Similar siderophile behaviours of H₂O are also observed in the two-phase simulations, from which the calculated $D_{\rm H_2O}^{\rm Fe/MgSiO_3}$ are ~9 and 3 at 500 and 1,000 GPa, respectively, in good agreement with the TI results (Extended Data Fig. 4).

Under given pressures, we find that $D_{\rm H_2O}^{\rm Fe/MgSiO_3}$ only marginally increases with decreasing temperature (Extended Data Fig. 3). For example, at $X_{\rm H_2O}^{\rm Fe}$ = 1.67 wt%, $D_{\rm H_2O}^{\rm Fe/MgSiO_3}$ increases from 8.4 to 9.9 with temperature decreasing from 14,200 K to 13,000 K at 1,000 GPa, and the increase is even smaller (-1) at 500 GPa with temperature decreasing from 9,800 K to 8,600 K. We combined our data with previous lower-pressure results and parameterized $D_{\rm H_2O}^{\rm Fe/MgSiO_3}$ as a function of $X_{\rm H_2O}^{\rm Fe}$ and pressure (*P*) (Fig. 1b). The temperature dependence was taken into account by correcting our calculated $D_{\rm H_2O}^{\rm Fe/MgSiO_3}$ to the values at the target temperatures, which are determined by the solidus of silicates 15,16 and melting curve of iron 17. We find that $D_{\rm H_2O}^{\rm Fe/MgSiO_3}$ always increases with growing pressure, yet the rate of this increase declines rapidly (Fig. 1b). At pressures beyond 400 GPa, the increase becomes nearly imperceptible.

To quantify the effect of water partitioning on planet interiors, we consider four different interior scenarios (Fig. 2):

- 1. Rocky interior with no melting, and a separate water layer
- Rocky interior with (dry) melting in both mantle and core, and no water dissolution
- 3. Same as B except with water dissolution in mantle melts
- 4. Same as C except with water dissolution in core

Differences between scenarios A, B and C have been explored in detail in a previous study 8 . Characteristically, calculated radii are smallest when water is stored in both mantle and core (scenario D; Figs. 2 and 3a), as a consequence of replacing water from the surface to fit within the iron and silicate structure. The addition of water reduces the

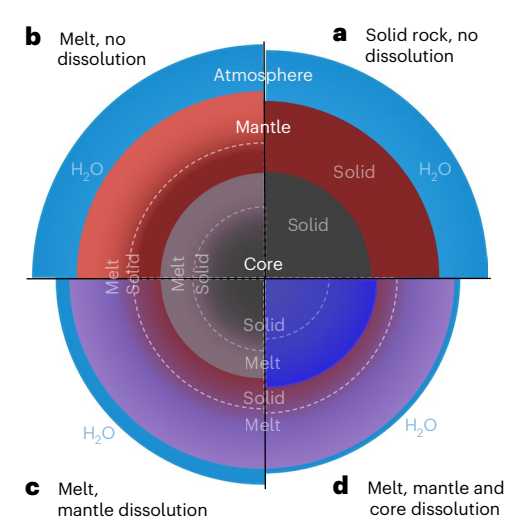


Fig. 2 | **Four model scenarios employed in our study. a**, Model A closely resembles models presented in refs. 69,70, and other commonly used exoplanet interior models follow model A where silicate melts are neglected. **b**, Model B is the model with melting in both mantle and core but without water dissolution. **c**, Model C represents the model with water dissolution in mantle melts. **d**, Model D with water dissolution in both mantle and core melts aligns closely with our current understanding of mineral physics and exoplanet interiors and is, therefore, the most accurate representation based on our existing knowledge. Core material is depicted in dark grey (solid and dry), light grey (molten and dry) or blue-purple (hydrous and solid or dry). Mantle material is depicted in dark red (solid and dry), light red (molten and dry) or light purple (molten and hydrous). Steam layers are depicted in blue. The dashed lines separate molten from solid phases.

density of both silicates and iron (Extended Data Fig. 5). Storing water deep in the interior implies that less water is available at the surface to act as a greenhouse gas, which lowers the surface temperature and, hence, the temperature of the interior. Meanwhile, water depresses the melting point. The interplay of these two effects of water results in the deep magma oceans observed in scenarios C and D (Extended Data Fig. 5). Figure 3 shows that the relative difference between scenario D and others depends on bulk water content and planetary mass. For a bulk water mass fraction (WMF) of 3 wt%, we observe a relative difference in planet radius of up to 25%, while WMFs of 20 wt% and 50 wt% exhibit differences of up to 14% (Fig. 3b). These differences are drastic compared with the observational uncertainties of well-characterized planets (down to a few per cent in density). We note that the case of 50% bulk water mass fraction is an end member in planet formation scenarios.

Planetary cores generally occupy a smaller volume than planetary mantles, at least for Earth-like rocky compositions and the generally anticipated range of rocky interiors¹⁸. Volumetrically speaking, the core is a smaller water reservoir than the mantle. However, iron can accommodate up to 70 times more water than silicates, depending on pressure and bulk water content. The net effect is that water is predominantly stored in the mantle for small-mass planets (below ~6 M_{\oplus}) and predominantly stored in the core for more massive planets (Fig. 4). Hence, for the majority of observed exoplanets, most of bulk planetary water is stored deep in their cores. For example, a 9 ${\rm M}_{\oplus}$ planet at T_{eq} = 1,000 K with a bulk water mass fraction of 50% will host 56% of the total water in the core, 41% in the mantle and only the remaining 3%on the surface. As the partitioning of water between iron and silicates is pressure sensitive, the distribution of water in planets is closely linked to the planet's mass. For a hot Earth-mass planet ($T_{eq} = 700 \text{ K}$) with a 75 times greater water inventory than the present-day surface water on Earth (0.023%), we find that 58.4% of total water resides in the core, 40.1% in the mantle and 1.4% on the surface, which corresponds to 0.024% of the total mass. This value is similar to the actual estimate of 0.023% water on Earth's surface. However, note that outgassing/ingassing and atmospheric loss to space can alter the initial surface water reservoir over the geological time. Here, we present static interior models in equilibrium states, where the net influx/outflux from the interior is zero.

Our interior model D is suited for warm and hot worlds inside the runaway greenhouse transition, where the presence of global magma oceans is expected. This scenario is particularly relevant for the majority of super-Earths and sub-Neptunes^{8,19}. Compared with previous interior interpretations of observed exoplanets, our results from model D imply that planets may be more water-rich than previously thought, as commonly used mass-radius relationships overestimate the total radius for a given bulk water mass fraction (scenarios A and B). As a result, inferred water mass budgets from observed mass-radius data can differ notably, with potential variations of up to nearly an order of magnitude (for example, as seen in the overlap of red and blue curves for 3% and 20% WMF in Fig. 3a). Overall, our results on water partitioning between iron and silicate melt have fundamental implications for the distribution of water within planets, their densities and thermal structures, surface conditions and, ultimately, their mass-radius relations.

The case of 55 Cnc e

The enigmatic nature of 55 Cnc e, an extremely irradiated super-Earth with an unusually low density $(M_p = 8.59 \pm 0.43 \,\mathrm{M}_{\oplus}, T_{\rm eq} \approx 2,000 \,\mathrm{K})^{20}$ continues to captivate the community. Various models have been proposed to account for its large radius R_p = 1.947 ± 0.038 R_{\oplus} in relation to its mass, including nitrogen-rich, hydrogen-rich or thin-metal-rich atmospheres on top of a magma ocean^{21,22} or an exotic rocky interior depleted in iron and enriched in Na and Ca²³. Water, if present on the surface, is expected to be in a state of loss. Observations in Ly-alpha of any extending atmosphere do not show any signals²⁴, which puts a low likelihood on the presence of surface water, although this could not be ruled out. In an extreme case, if 55 Cnc e lost all its mantle and surface water, but still holds water deep in its core, we can fit the mass-radius data with a water mass fraction of 34%, resulting in a radius of 1.946 R_{\oplus} for a mass of $M_p = 8.59$, assuming an Earth-like core-mantle ratio. This amount corresponds to an initial bulk water budget of 55 Cnc e of much more than the usually assumed upper limit of 50% just after the planet's formation (Fig. 4). If we assume the equilibration between silicates and iron happens at higher pressures, for example, the pressure at the coremantle boundary (CMB), this initial bulk water budget decreases to 45%. If this scenario holds true, it would indicate that the planet formed from water-rich building blocks originating from beyond the ice line. Further investigations with evolution models are necessary to address whether this low-density planet can have water deep in its interior and whether this scenario requires a tenuous amount of surface water to still be exposed at the surface. In comparison with Dorn and Lichtenberg⁸, we find that the majority of water in 55 Cnc e must be in the core and not in the mantle. This is an important difference, as water can be outgassed from the mantle, while it is locked up in the core for its lifetime.

Sub-Neptunes

The nature of sub-Neptunes is debated. Given mass and radius, the interiors of sub-Neptunes are degenerate. Hydrogen-dominated envelopes and water-rich interiors are discussed²⁵. There are drawbacks to water-rich interiors despite the fact that they can fit the densities²⁶ and close-in water-rich worlds are predicted in planetary formation studies²⁷. Mainly, the water world scenario does not explain two key observed correlations: radius distribution with orbital period and the bulk densities with stellar irradiation²⁵. The presence of hydrogen-dominated envelopes remains the best explanation for their interiors as the two key observed correlations can be matched. In light of this, we compare our resulting mass-radius curves with the

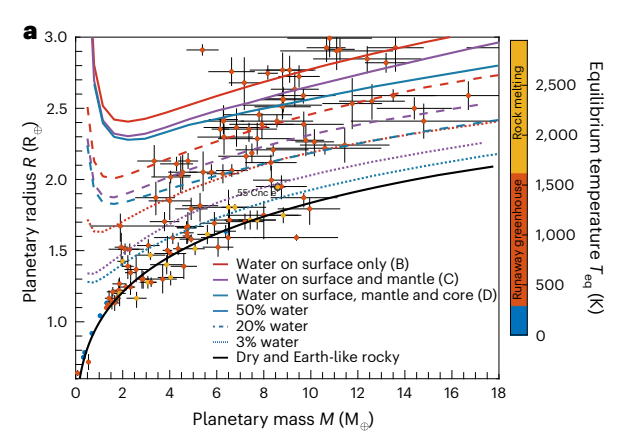
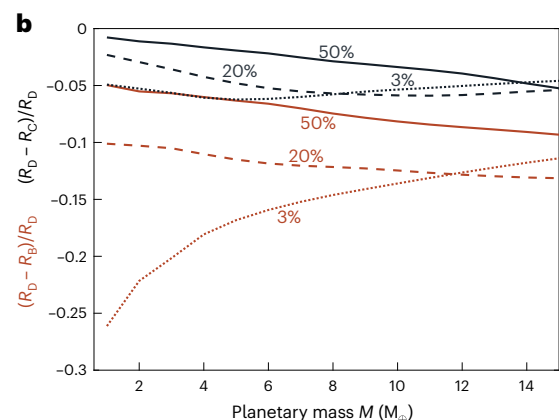


Fig. 3 | **The effect of water partitioning into the core and mantle on mass-radius relationships. a**, Mass-radius relation of exoplanets under various bulk water content and interior models (black, D versus C; red, D versus B following Fig. 2). Data with 1 sigma error bars for well-characterized exoplanets are shown for comparison. b, Differences in calculated planet radii as a function of bulk water content, interior model and planetary mass (radii for interior models D, C and B are denoted $R_{\rm D}$, $R_{\rm C}$ and $R_{\rm B}$). The results are shown relative to the scenario D, the most self-consistent interior model. The rocky interior is composed of Mg–Si oxides and silicates (66 wt%) and an iron core of 33 wt% (see black line for a dry interior). We add different amounts of water (3%, 20% and 50% of the



total mass fraction). All curves are shown for an equilibrium temperature of 1,000 K. The planet sample comes from the PlanetS database 71 (as of June 2023) to which we have added TOI-561b, c and d^{72} and the new estimates for Kepler-138 d, c and e^{73} . We show planets with mass uncertainties better than 35% and radius uncertainties better than 30%. Differences between the model scenarios range from 3% to 25%. When neglecting water dissolution in the mantle and core, the errors are the largest. The largest errors are identified for small planet masses and lower water mass fractions, similar to what has been shown for the water dissolution in the mantle 8 . For equilibrium temperatures, an albedo of 0.4 is assumed.

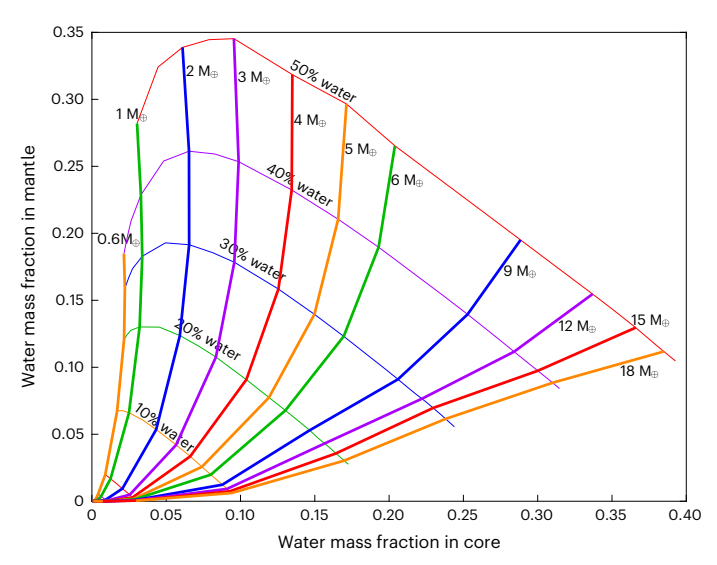


Fig. 4 | **Water mass fractions stored in the mantle and the core depending on planet mass (thick lines) and bulk water mass fraction (thin lines).** As the partitioning of water is pressure dependent, the distribution of water within planets depends strongly on planet mass. The residual amount of water that is not stored in either mantle or core is kept on the surface. All lines have been calculated assuming an equilibrium temperature of 1,000 K, and we note that the effect of temperature is negligible for the planets of interest. Different colours are used only for readability.

observed sub-Neptune population. Planets above $2.5\,R_\oplus$ require the addition of a hydrogen (Fig. 3) unless they could be more water-rich than 50%, which is difficult. Our 50% bulk water curve levels out around $2.5\,R_\oplus$ for higher masses and a 1,000 K equilibrium temperature. As the majority of sub-Neptunes have equilibrium temperatures below 1,000 K, it is a conservative estimate. For example, GJ 1214 b^{28} is unlikely to be a water world as previously suggested. Its radius of 2.742 R_\oplus is about 7 sigma higher than that of the 50% water world scenario with $2.4\,R_\oplus$ at its equilibrium temperature of 596 K. We can expect hydrogen

in its atmosphere, which is advantageous for JWST observations as it increases the atmospheric scale height.

Water-rich planets

Recently, a class of water-rich planets around M dwarfs has been proposed. The six planets considered roughly follow a curve calculated for a composition of 50% water and 50% silicates (for $T_{\rm eq}$ = 300 K). As the equilibrium temperatures of the six planets vary between 387 K and 1,069 K, and the extent of water atmospheres is highly temperature dependent within this range, we calculated different mass-radius relationships with scenario D. Clearly, the planet sample does not follow a single mass-radius curve (Fig. 5), indicating diversity among these exoplanets, probably with bulk water mass fractions ranging from 10% to 40%. All six planets have densities higher than the densities of planets with 50% water. Besides water, the radii may also partly be explained by moderate-sized hydrogen-dominated envelopes. However, hydrogen-dominated atmospheres might only be possible in a narrow parameter space, especially on super-Earths smaller than ~7 M_{\oplus} (ref. 30).

Our results also have important implications for the potential habitability of water-rich worlds. Previous studies have suggested that super-Earths with too much water are unlikely to develop habitable surface conditions³¹, as a solid layer of water may separate liquid water from silicate minerals in the mantle^{32,33}. However, our findings imply that worlds with thick water layers may not be common, as the majority of water on super-Earths will probably be locked in the interior instead of the surface, especially for more massive planets (Fig. 4). Hence, even water-rich planets that formed initially with tens of water mass fractions may have the potential to develop Earth-like surface conditions. Future studies need to assess these implications quantitatively. Our research thus opens up new possibilities for understanding the habitability of exoplanets and sheds light on the potential existence of water-rich worlds that can support life.

Methods

Calculations of chemical potentials and partition coefficients The method of calculating the chemical potential of H_2O in iron (Fe)/silicate (MgSiO₃) melt is outlined in detail in previous studies ^{9,13} and is

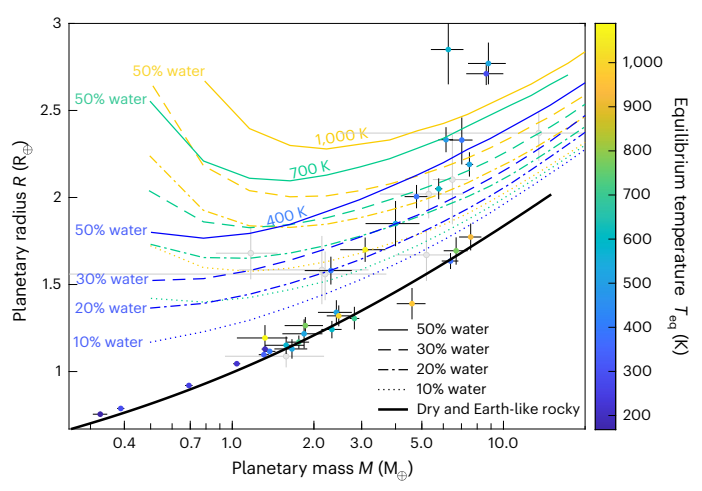


Fig. 5 | Mass-radius curves compared with the sample of small transiting planets around M dwarfs from Luque and Pallé²⁹. All curves are calculated using scenario D, if not mentioned otherwise. Coloured curves are calculated for different equilibrium temperatures and different water mass fractions (see line styles). The curves at 1,000 K and 3%, 20% and 50% water mass fractions are also shown in Fig. 3, as is the solid black line. The planets previously interpreted to be water-rich $(-50\%)^{29}$ are likely to be more diverse in composition and contain less than 50% of water. The 1 sigma error bars for the planets are shown.

briefly summarized here. The Gibbs free energy of a system at specific pressure (P), temperature (T) and solute concentration (x) can be written as

$$G(p,T,x) = \bar{G}(p,T,x) - TS_{\text{mix}}^{\text{system}},$$
(1)

where $\bar{G}(p,T,x)$ is the excess free energy and $S_{\text{mix}}^{\text{system}}$ is the ideal gas mixing entropy. Then, the chemical potential of H_2O can be expressed as

$$\mu_{H_2O}(p, T, x) = \bar{\mu}_{H_2O}(p, T, x) - TS_{mix}^{H_2O}.$$
 (2)

Here, $\bar{\mu}_{H_2O}(p, T, x)$ and $S_{mix}^{H_2O}$ can be calculated by

$$\bar{\mu}_{\mathrm{H}_{2}\mathrm{O}}\left(p,T,x\right) = \bar{G}\left(p,T,x\right) + (1-x)\frac{\partial \bar{G}\left(p,T,x\right)}{\partial x} \tag{3}$$

$$S_{\text{mix}}^{\text{H}_2\text{O}} = S_{\text{mix}}^{\text{system}} + (1 - x) \frac{\partial S_{\text{mix}}^{\text{system}}}{\partial x}$$
 (4)

The variations of $\bar{G}(p,T,x)$ per formula with respect to x for our systems, $\mathrm{Fe_{1-x}(H_2O)_x}$ and $\mathrm{(MgSiO_3)_{1-x}(H_2O)_x}$, were found to be fitted well using a linear equation:

$$\bar{G}(p, T, x) = a + bx,\tag{5}$$

where a and b are the fitting parameters. As a result, $\bar{\mu}_{\text{H}_2\text{O}}$ (p, T, x) can be calculated as a+b and the errors of $\bar{\mu}_{\text{H}_2\text{O}}$ (p, T, x) can be derived using error propagation based on the uncertainties of a and b.

The $S_{\text{mix}}^{H_2O}$ for the two systems calculated using equation (4) are

$$S_{\text{mix}}^{\text{H}_2\text{O in Fe}} = -k_{\text{B}} \left(2\ln \frac{2x}{1+2x} + \ln \frac{x}{1+2x} \right)$$
 (6)

$$S_{\text{mix}}^{\text{H}_2\text{O in MgSiO}_3} = -k_{\text{B}} \left(2\ln \frac{2x}{5 - 2x} + \ln \frac{3 - 2x}{5 - 2x} \right),$$
 (7)

where $k_{\rm B}$ is the Boltzmann constant. Then, at equilibrium when $\mu_{\rm H_2O}^{\rm Fe}(p,T,x)=\mu_{\rm H_2O}^{\rm MgSiO_3}(p,T,y)$, the partition coefficients $D_{\rm H_2O}^{\rm Fe/MgSiO_3}=x/y$ can be easily derived using equation (2).

Molecular dynamics simulations

We simulated iron melts and silicate melts using supercells consisting of 64 Fe atoms and 32 formulae of MgSiO₃, respectively. H₂O was later added to the supercells for water-bearing systems. Born-Oppenheimer ab initio molecular dynamics simulations were conducted using the projector augmented wave method^{34,35} and PBEsol exchange-correlation functional³⁶, as implemented in the Vienna Ab initio Simulation Package (VASP)³⁷. The valence configurations we used for elements are Fe $3p^63d^74s^1$, Mg $2p^63s^2$, Si $3s^23p^2$, O $2s^22p^4$ and H $1s^1$. Ions and electrons were assumed to be in thermal equilibrium via the Mermin functional³⁸. We ran each simulation up to 20,000 steps with a timestep of 0.5 fs. Gamma point Brillouin zone sampling and a plane wave energy cut-off of 600 eV and 800 eV for iron and silicate melts, respectively, were initially utilized. We then corrected the pressure for iron by employ $ing 2 \times 2 \times 2$ Monkhorst-Pack mesh of k points, as the system size we used for iron is small. A canonical ensemble (NVT) with temperature controlled by a Nosé-Hoover thermostat was adopted³⁹. To determine the equilibrium volume, we performed several NVT simulations using different volumes around the target pressure and then fitted the pressure-volume data. Radial distribution function and mean-square displacement were examined to make sure that our simulated systems were in the liquid state.

Thermodynamic integration

We calculated the Gibbs free energy of iron and silicate melts by TI from ideal gas 40 . To do this, the difference in internal energy between the melt (U_1) and the ideal gas (U_0) with respect to the coupling parameter λ is integrated by

$$\Delta G_{0-1} = \int_0^1 \mathrm{d}\lambda \langle U_1(R) - U_0(R) \rangle_{\lambda}. \tag{10}$$

To overcome the numerical instabilities resulting from close contacts between non-interacting atoms at $\lambda = 0$, we employed the variable transformation approach²⁸ with $\lambda(x) = \left(\frac{x+1}{2}\right)^{1/(1-k)}$, which yields

$$\Delta G = \frac{1}{2(1-\kappa)} \int_{-1}^{1} f(\lambda(x)) \lambda(x)^{k} dx, \tag{11}$$

where we adopted k=0.8. We used an 8-point Gauss–Lobatto rule to evaluate this integral. The errors of internal energies were calculated by blocking average method⁴¹. We obtained the errors of the numerically integrated free energies by error propagation. We also examined the use of the Weeks–Chandler–Andersen fluid as the reference state for the liquid, rather than the ideal gas, and found that the discrepancy in free energies is minimal. Additionally, we anticipate that more intricate integrated pathways are unlikely to significantly alter our partitioning outcomes, as they typically yield only marginal differences in free energy, on the order of tens of millielectronvolts per atom⁴². This disparity is approximately one order of magnitude smaller than the error bar associated with the chemical potential. The Gibbs free energy of the ideal gas was calculated as

$$G^{ig} = F^{ig} + PV = -k_B T \sum_i \ln\left(\frac{V^{N_i}}{N_i! \Lambda_i^{3N_i}}\right) + PV, \tag{12}$$

where $k_{\rm B}$ is the Boltzmann constant, T is the temperature, P is the pressure, V is the volume, N_i is the number of atoms for element i, and Λ_i is the thermal wavelength of element i given by $\Lambda_i = h/(2\pi M_i k_{\rm B} T)^{\frac{1}{2}}$, with h

being the Plank's constant and M_i being the atomic mass of element i. We calibrated all the calculations to the target pressures using the thermodynamic relation

$$G(P_2, T) - G(P_1, T) = \left(\int_{P_1}^{P_2} V dP\right)_T$$
 (13)

Planet interior calculations

We employ a one-dimensional interior model that describes a planet in hydrostatic equilibrium that incorporates three components: a core, a mantle and a water layer (of steam, liquid, solid or supercritical). We solve the equation of mass conservation, the equation of hydrostatic equilibrium, the equation of thermal transport and the equation of states for different materials/phases. Our model is built upon Dorn and Lichtenberg 8 , with major improvements that include the equation of states for dry and wet iron melts and the dissolution of water in the core. For the scope of this study, we exclude an atmosphere of other species of high mean molecular weight or H/He, and the only volatile considered is $\rm H_2O$.

The core

We consider a core made of Fe, H and O. For solid Fe, we use the equations of state for hexagonal close packed (hcp) iron at $P \ge 310$ GPa (ref. 43) and at P < 310 GPa (ref. 44). For liquid iron and liquid iron with H_2O , we perform ab initio molecular dynamics simulations and calculate their equations of state (PVT) under the extreme pressure and temperature conditions relevant to super-Earths and sub-Neptunes (-8,000–14,000 K and -50–1,300 GPa). The Mie–Grüneisen equation of state for dry liquid iron (64 Fe atoms) and hydrous liquid iron (64 Fe atoms and 8 H_2O) can be expressed as

$$P = \frac{3}{2} K_{T_0} \left[\left(\frac{V_0}{V} \right)^{\frac{7}{3}} - \left(\frac{V_0}{V} \right)^{\frac{5}{3}} \right] \left[1 + \frac{3}{4} (K'_{T_0} - 4) \right]$$

$$\left\{ \left(\frac{V_0}{V} \right)^{\frac{2}{3}} - 1 \right\} + \frac{(T - T_0)}{1,000} \left[a + b \left(\frac{V_0}{V} \right) + c \left(\frac{V_0}{V} \right)^2 \right],$$
(14)

where, for dryliquidiron, $K_{T_0}=49.249\,\mathrm{GPa}$, $K_{T_0}'=4.976$, $V_0=1,043.912\,\mathrm{\mathring{A}}^3$, $T_0=8,000\,\mathrm{K}$, a=-15.957, b=20.946 and c=-3.811. For hydrous liquidiron, $K_{T_0}=57.162\,\mathrm{GPa}$, $K_{T_0}'=4.535$, $V_0=1,181.389\,\mathrm{\mathring{A}}^3$, $T_0=8,000\,\mathrm{K}$, a=-8.478, b=12.049 and c=-1.258. The phase transitions are calculated following Anzellini et al. ⁴⁵. The melting curve is calculated following recent experimental ¹⁷ and computational ⁴⁶ works by assuming a linear H and O concentration dependence: $T_m=T_{m,\mathrm{hcp,Fe}}=a_1x-b_1y$, where $a_1=1,031\,\mathrm{K}$ and $b_1=100\,\mathrm{K}$, and $T_{m,\mathrm{hcp,Fe}}=5,530\times((P-260)/293+1)^{0.552}$. The parameter x is the mass fraction of H in wt%, and y is the mass fraction of O in wt%.

The core thermal profile is assumed to be adiabatic throughout the core. At the CMB, there is a temperature jump as the core can be hotter than the mantle owing to the residual heat released during core formation. Following Stixrude¹⁵, this temperature jump depends on the melting temperature of the silicate mantle. If the initially calculated temperature at the CMB is lower than the melting temperature of the mantle material, the CMB temperature is increased up to the melting temperature. However, in most of our simulations, the mantle is fully molten and, thus, no temperature jump is imposed at the CMB.

The mantle

The calculation of the mantle structure is described in detail in Dorn and Lichtenberg⁸, with few adaptations. In brief, the mantle is assumed to be made up of three major components: MgO, SiO₂ and FeO. For the solid mantle, we use the thermodynamical model Perple_X⁴⁷ to compute stable mineralogy and density for a given composition, pressure and temperature, employing the database of Stixrude and Lithgow-Bertelloni⁴⁸. For pressures higher than -125 GPa, we define stable minerals a priori and use their respective equation of states from various sources^{48–51}. We consider SiO₂ from Faik et al.⁵¹, post-perovskite (Mg, Fe)SiO₃ from Hemley et al.⁵², FeO from Fischer et al.⁴⁹ and MgO from Musella et al.⁵⁰. For the liquid mantle, we calculate its density assuming an ideal mixture of components as in Dorn and Lichtenberg⁸. Specifically, we use the equations of state for Mg₂SiO₄ from Stewart et al.⁵³, for SiO₂ at $P \ge 20$ GPa from Faik et al.⁵¹, for SiO₂ at

P < 20 GPa from Melosh⁵⁴ and for FeO from Ichikawa and Tsuchiya⁵⁵. To compute mixtures of the above components, we use the additive volume law⁵³. We use Mg₂SiO₄ instead of MgO since the data for forsterite have been recently updated for the high-pressure temperature regime, which is not available for MgO to our knowledge.

The addition of water reduces the density, for which we follow Bajgain et al. 56 and reduce the silicate density by $0.036\,\mathrm{g\,cm^{-3}}$ per wt% water. For small water mass fractions, this reduction is nearly independent of pressure and temperature. At large water mass fractions, a constant density reduction becomes invalid. Thus, we also calculate the density of the rock–water mixture with the additive volume law and use the maximum density of both values.

The water layer

Water can be in solid, liquid, steam or supercritical phase. We use the equation of state compilation of Haldemann et al. 59 . The transit radius of a planet is assumed to be at a pressure of $P_{\rm Transit}$ = 1 mbar. This is a simplification as the transit radius depends on temperature, while its effect on the planets of interest is small 60 . The thermal profile is assumed to be fully adiabatic, except for pressures smaller than the pressure at the tropopause, which we fix at 0.1 bar and where we keep an isothermal profile as in Dorn and Lichtenberg 8 . Note that we simply consider sub-Neptunes as planets with sizes greater than two times the radius of Earth. Our model does not take into account the potential presence of universal H/He atmospheres in sub-Neptunes.

Water-melt mixtures

For the model scenarios C and D, we allow the water to be mixed into the mantle melt, and both mantle and core melts, respectively. The partitioning between mantle melts and the water layer is determined by a modified Henry's law, for which empirical data are input and summarized in Bower et al. (<300 bar), Lichtenberg et al. (<1 GPa) and Kessel et al. (for the second critical endpoint). We use a fitted solubility function, which can be found in Dorn and Lichtenberg. For the partitioning of water between iron and silicates, we follow the dependencies as described in the main text (see also Fig. 1). For the equilibration pressure, we use half of the CMB pressure.

Water plays a crucial role in melt processes. As described above, we account for the effect of water in reducing the melting temperature and melt density. In principle, water can also be taken up by solid rocks. However, the solubility of water in solid rocks is orders of magnitude lower than in melts. Thus, we neglect the effect of hydrated solid silicates on the total radius as it accounts for only a few per cent at maximum and only in extreme cases⁶³.

Oxidation of iron

 $\rm H_2O$ may act as an oxidizing agent in the planetary interior. The possibility of fully oxidizing metallic iron by water to form coreless exoplanets was discussed 64 while explicitly assuming that water oxidizes iron. Indeed, FeO is expected in water-rich planetesimals in the form of clays at low temperature 65 . However, these FeO-rich clays destabilize at higher temperatures before melting occurs (beyond $^{-1}$,000 K) 66 . During the magma ocean stage, the extent of iron oxidation involves a dynamic interplay between the rate of oxidation, the rate at which the metallic iron descends, the size of the metal drop and the reactions between different species such as $\rm H_2$, $\rm H_2O$, Fe and FeO. We show below that the effect of iron oxidation (if any) on the mass–radius relationship is relatively small. In fact, iron oxidation

would lead to a further decrease in the radius compared with the scenario D we consider.

First, the thermodynamic modelling suggests that both water and metallic iron may be produced via the redox reactions between primordial hydrogen and mantle melts 6 . More specifically, the reaction such as $FeO_{silicate} + H_{2.silicate} \leftrightharpoons Fe_{metal} + H_2O_{silicate}$ may initially lean towards the right-hand side for super-Earths and sub-Neptunes, which suggests that (1) iron reduction, rather than oxidation, is dominant during the core formation and (2) our calculations are relevant also for planets whose water originates from endogenic water in addition to primordially accreted water.

Second, it is found that the equations of state (PVT) of Mg_{1-x}Fe_xSiO₃ liquid is very similar to that of pure MgSiO₃ liquid⁶⁷. Therefore, even if a big chunk of iron is oxidized, the presence of oxidized ferrous iron in the silicate melt may not have a significant influence on our calculated metal-silicate partition coefficients of water. While our calculations realistically quantify the water concentration in the core, the size and the mass of the core may be affected by iron oxidation. To investigate the effect of iron oxidation on calculated radii, we extrapolate the partitioning coefficients to the extreme case of 50% bulk water mass fraction. Because it remains unknown at the core formation conditions of super-Earths how much iron is oxidized given a bulk water mass fraction, we directly add different amounts of iron as mantle FeO for the 50% bulk water case and keep the total amount of oxygen constant (Supplementary Fig. 2). In cases where water oxidizes less than 50% of the iron as mantle FeO, the decrease in total radius is less than 2%. If water oxidizes more than 50% of the iron, the radius decrease is notable (up to 10%). We highlight that the case of 50% bulk water mass fraction is an end member in planet formation scenarios⁶⁸.

Data availability

Authors can confirm that all relevant data are included in the Article and Supplementary Information files. Data used in the figures and our raw simulation outputs are available from figshare at https://doi.org/10.6084/m9.figshare.25800577 (ref. 74).

Code availability

The VASP is a proprietary software available for purchase at https://www.vasp.at/. The code for performing planetary interior modelling is available from the corresponding authors on reasonable request.

References

- Fegley, B., Lodders, K. & Jacobson, N. S. Volatile element chemistry during accretion of the earth. Geochem. 80, 125594 (2020).
- Boley, K. M. et al. Fizzy super-Earths: impacts of magma composition on the bulk density and structure of lava worlds. Astrophys. J. 954, 202 (2023).
- Raymond, S. N. & Morbidelli, A. in Demographics of Exoplanetary Systems: Lecture Notes of the 3rd Advanced School on Exoplanetary Science (eds Biazzo, K. et al.) 3–82 (Springer, 2022).
- Kite, E. S. & Barnett, M. N. Exoplanet secondary atmosphere loss and revival. Proc. Natl Acad. Sci. USA 117, 18264–18271 (2020).
- Vazan, A., Sari, R. & Kessel, R. A new perspective on the interiors of ice-rich planets: ice-rock mixture instead of ice on top of rock. Astrophys. J. 926, 150 (2022).
- Schlichting, H. E. & Young, E. D. Chemical equilibrium between cores, mantles, and atmospheres of super-Earths and sub-Neptunes and implications for their compositions, interiors, and evolution. *Planet. Sci. J.* 3, 127 (2022).
- Lichtenberg, T. et al. Vertically resolved magma oceanprotoatmosphere evolution: H₂, H₂O, CO₂, CH₄, CO, O₂, and N₂ as primary absorbers. J. Geophys. Res. Planets 126, e2020JE006711 (2021).
- Dorn, C. & Lichtenberg, T. Hidden water in magma ocean exoplanets. Astrophys. J. Lett. 922, L4 (2021).

- Li, Y. G., Vocadlo, L., Sun, T. & Brodholt, J. P. The Earth's core as a reservoir of water. Nat. Geosci. 13, 453–458 (2020).
- Yuan, L. & Steinle-Neumann, G. Strong sequestration of hydrogen into the Earth's core during planetary differentiation. Geophys. Res. Lett. 47, e2020GL088303 (2020).
- 11. Tagawa, S. et al. Experimental evidence for hydrogen incorporation into Earth's core. *Nat. Commun.* **12**, 2588 (2021).
- Yuan, L. & Steinle-Neumann, G. Possible control of Earth's boron budget by metallic iron. Geophys. Res. Lett. 49, e2021GL096923 (2022).
- Li, Y. G., Vocadlo, L., Ballentine, C. & Brodholt, J. P. Primitive noble gases sampled from ocean island basalts cannot be from the Earth's core. Nat. Commun. 13, 3770 (2022).
- Deng, J. & Du, Z. Primordial helium extracted from the Earth's core through magnesium oxide exsolution. Nat. Geosci. 16, 541–545 (2023).
- Stixrude, L. Melting in super-Earths. *Phil. Trans. R. Soc. A* 372, 20130076 (2014).
- Fei, Y. W. et al. Melting and density of MgSiO₃ determined by shock compression of bridgmanite to 1254GPa. *Nat. Commun.* 12, 876 (2021).
- 17. Kraus, R. G. et al. Measuring the melting curve of iron at super-Earth core conditions. *Science* **375**, 202–205 (2022).
- Unterborn, C. T. et al. The nominal ranges of rocky planet masses, radii, surface gravities, and bulk densities. Astrophys. J. 944, 42 (2023).
- 19. Luger, R. & Barnes, R. Extreme water loss and abiotic O_2 buildup on planets throughout the habitable zones of M dwarfs. *Astrobiology* **15**, 119–143 (2015).
- 20. Crida, A., Ligi, R., Dorn, C. & Lebreton, Y. Mass, radius, and composition of the transiting planet 55 Cnc e: using interferometry and correlations. *Astrophys. J.* **860**, 122 (2018).
- 21. Ridden-Harper, A. R. et al. Search for an exosphere in sodium and calcium in the transmission spectrum of exoplanet 55 Cancri e. *Astron. Astrophys.* **593**, A129 (2016).
- Hammond, M. & Pierrehumbert, R. T. Linking the climate and thermal phase curve of 55 Cancri e. Astrophys. J. 849, 152 (2017).
- Dorn, C., Mosegaard, K., Grimm, S. L. & Alibert, Y. Interior characterization in multiplanetary systems: TRAPPIST-1. Astrophys. J. 865, 20 (2018).
- Bourrier, V. et al. The 55 Cancri system reassessed. Astron. Astrophys. 619, A1 (2018).
- Bean, J. L., Raymond, S. N. & Owen, J. E. The nature and origins of sub-Neptune size planets. J. Geophys. Res. Planets 126, e2020JE006639 (2021).
- Mousis, O. et al. Irradiated ocean planets bridge super-Earth and sub-Neptune populations. Astrophys. J. Lett. 896, L22 (2020).
- Emsenhuber, A. et al. Realistic on-the-fly outcomes of planetary collisions. II. Bringing machine learning to N-body simulations. Astrophys. J. 891, 6 (2020).
- Cloutier, R., Charbonneau, D., Deming, D., Bonfils, X. & Astudillo-Defru, N. A more precise mass for GJ 1214 b and the frequency of multiplanet systems around mid-M dwarfs. Astron. J. 162, 174 (2021).
- 29. Luque, R. & Pallé, E. Density, not radius, separates rocky and water-rich small planets orbiting M dwarf stars. *Science* **377**, 1211–1214 (2022).
- 30. Hu, R., Gaillard, F. & Kite, E. S. Narrow loophole for H_2 -dominated atmospheres on habitable rocky planets around M dwarfs. Astrophys. J. Lett. **948**, L20 (2023).
- 31. Maruyama, S. et al. The naked planet Earth: most essential pre-requisite for the origin and evolution of life. *Geosci. Front.* **4**, 141–165 (2013).
- Noack, L. et al. Water-rich planets: how habitable is a water layer deeper than on Earth? *Icarus* 277, 215–236 (2016).

- 33. Léger, A. et al. A new family of planets? 'Ocean-Planets'. *Icarus* **169**, 499–504 (2004).
- Blochl, P. E. Projector augmented-wave method. *Phys. Rev. B* 50, 17953–17979 (1994).
- Kresse, G. & Joubert, D. From ultrasoft pseudopotentials to the projector augmented-wave method. *Phys. Rev. B* 59, 1758–1775 (1999).
- Perdew, J. P. et al. Restoring the density-gradient expansion for exchange in solids and surfaces. *Phys. Rev. Lett.* 100, 136406 (2008).
- Kresse, G. & Furthmüller, J. Efficiency of ab-initio total energy calculations for metals and semiconductors using a plane-wave basis set. Comput. Mater. Sci. 6, 15–50 (1996).
- 38. Mermin, N. D. Thermal properties of the inhomogeneous electron gas. *Phys. Rev.* **137**, A1441–A1443 (1965).
- Nosé, S. A unified formulation of the constant temperature molecular dynamics methods. J. Chem. Phys. 81, 511–519 (1984).
- Dorner, F., Sukurma, Z., Dellago, C. & Kresse, G. Melting Si: beyond density functional theory. *Phys. Rev. Lett.* 121, 195701 (2018).
- 41. Flyvbjerg, H. & Petersen, H. G. Error estimates on averages of correlated data. *J. Chem. Phys.* **91**, 461–466 (1989).
- González-Cataldo, F. & Militzer, B. Ab initio determination of iron melting at terapascal pressures and super-Earths core crystallization. *Phys. Rev. Res.* 5, 033194 (2023).
- Hakim, K. et al. A new ab initio equation of state of hcp-Fe and its implication on the interior structure and mass-radius relations of rocky super-Earths. *Icarus* 313, 61–78 (2018).
- 44. Miozzi, F. et al. A new reference for the thermal equation of state of iron. *Minerals* **10**, 100 (2020).
- Anzellini, S., Dewaele, A., Mezouar, M., Loubeyre, P. & Morard, G. Melting of iron at Earth's inner core boundary based on fast X-ray diffraction. Science 340, 464–466 (2013).
- He, Y. et al. Superionic iron alloys and their seismic velocities in Earth's inner core. *Nature* 602, 258–262 (2022).
- 47. Connolly, J. A. D. The geodynamic equation of state: what and how. *Geochem. Geophys. Geosyst.* **10**, Q10014 (2009).
- Stixrude, L. & Lithgow-Bertelloni, C. Thermal expansivity, heat capacity and bulk modulus of the mantle. *Geophys. J. Int.* 228, 1119–1149 (2022).
- Fischer, R. A. et al. Equation of state and phase diagram of FeO. Earth Planet. Sci. Lett. 304, 496–502 (2011).
- 50. Musella, R., Mazevet, S. & Guyot, F. Physical properties of MgO at deep planetary conditions. *Phys. Rev. B* **99**, 064110 (2019).
- Faik, S., Tauschwitz, A. & Iosilevskiy, I. The equation of state package FEOS for high energy density matter. *Comput. Phys. Commun.* 227, 117–125 (2018).
- 52. Hemley, R. J., Stixrude, L., Fei, Y. & Mao, H. K. Constraints on lower mantle composition from P-V-T measurements of (Fe, Mg) SiO₃-perovskite and (Fe, Mg)O. *Geophys. Monogr. Ser.* **67**, 183–189 (1992).
- Stewart, S. et al. The shock physics of giant impacts: key requirements for the equations of state. AIP Conf. Proc. 2272, 080003 (2020).
- Melosh, H. J. A hydrocode equation of state for SiO₂. Meteorit. Planet. Sci. 42, 2079–2098 (2007).
- 55. Ichikawa, H. & Tsuchiya, T. Ab initio thermoelasticity of liquid iron-nickel-light element alloys. *Minerals* **10**, 59 (2020).
- Bajgain, S., Ghosh, D. B. & Karki, B. B. Structure and density of basaltic melts at mantle conditions from first-principles simulations. *Nat. Commun.* 6, 8578 (2015).
- Belonoshko, A. B. et al. High-pressure melting of MgSiO₃. Phys. Rev. Lett. 94, 195701 (2005).

- 58. Katz, R. F., Spiegelman, M. & Langmuir, C. H. A new parameterization of hydrous mantle melting. *Geochem. Geophys. Geosyst.* **4**, 1073 (2003).
- Haldemann, J., Alibert, Y., Mordasini, C. & Benz, W. AQUA: a collection of H₂O equations of state for planetary models. Astron. Astrophys. 643, A105 (2020).
- 60. Turbet, M. et al. A review of possible planetary atmospheres in the TRAPPIST-1 system. *Space Sci. Rev.* **216**, 100 (2020).
- Bower, D. J., Hakim, K., Sossi, P. A. & Sanan, P. Retention of water in terrestrial magma oceans and carbon-rich early atmospheres. *Planet. Sci. J.* 3, 93 (2022).
- Kessel, R., Ulmer, P., Pettke, T., Schmidt, M. W. & Thompson, A. B. The water-basalt system at 4 to 6 GPa: phase relations and second critical endpoint in a K-free eclogite at 700 to 1400 degrees C. Earth Planet. Sci. Lett. 237, 873–892 (2005).
- 63. Shah, O., Alibert, Y., Helled, R. & Mezger, K. Internal water storage capacity of terrestrial planets and the effect of hydration on the M-R relation. *Astron. Astrophys.* **646**, A162 (2021).
- 64. Elkins-Tanton, L. T. & Seager, S. Coreless terrestrial exoplanets. Astrophys. J. **688**, 628–635 (2008).
- Johansen, A., Ronnet, T., Schiller, M., Deng, Z. B. & Bizzarro, M. Anatomy of rocky planets formed by rapid pebble accretion. I. How icy pebbles determine the core fraction and FeO contents. Astron. Astrophys. 671, A74 (2023).
- 66. Fu, R. R. & Elkins-Tanton, L. T. The fate of magmas in planetesimals and the retention of primitive chondritic crusts. *Earth Planet. Sci. Lett.* **390**, 128–137 (2014).
- 67. Karki, B. B., Ghosh, D. B., Maharjan, C., Karato, S. & Park, J. Density-pressure profiles of Fe-bearing MgSiO₃ liquid: effects of valence and spin states, and implications for the chemical evolution of the lower mantle. *Geophys. Res. Lett.* **45**, 3959–3966 (2018).
- Marounina, N. & Rogers, L. A. Internal structure and CO₂ reservoirs of habitable water worlds. Astrophys. J. 890, 107 (2020).
- Dorn, C. et al. Can we constrain the interior structure of rocky exoplanets from mass and radius measurements? Astron. Astrophys. 577, A83 (2015).
- Dorn, C. et al. A generalized Bayesian inference method for constraining the interiors of super Earths and sub-Neptunes. Astron. Astrophys. 597, A37 (2017).
- 71. Otegi, J. F., Bouchy, F. & Helled, R. Revisited mass-radius relations for exoplanets below 120 Mm. Astron. Astrophys. **634**. A43 (2020).
- 72. Lacedelli, G. et al. Investigating the architecture and internal structure of the TOI-561 system planets with CHEOPS, HARPS-N, and TESS. Mon. Not. R. Astron. Soc. **511**, 4551–4571 (2022).
- 73. Piaulet, C. et al. Evidence for the volatile-rich composition of a 1.5-Earth-radius planet. *Nat. Astron.* **7**, 206–222 (2023).
- Luo, H., Dorn, C. & Deng, J. Data and MD output for H₂O partitioning. *figshare* https://doi.org/10.6084/m9.figshare. 25800577 (2024).

Acknowledgements

The work reported in this paper was conducted using the Princeton Research Computing, which is a consortium of groups led by the Princeton Institute for Computational Science and Engineering (PICSciE) and the Office of Information Technology's Research Computing. J.D. acknowledges support from the National Science Foundation under grant no. EAR-2242946. C.D. acknowledges support from the Swiss National Science Foundation under grant TMSGI2_211313. In parts, this work has been carried out within the framework of the NCCR PlanetS supported by the Swiss National Science Foundation under grants 51NF40_182901 and 51NF40_205606 to C.D.

Author contributions

Conceptualization: J.D. and C.D. Methodology: H.L. and C.D. Investigation: H.L. and C.D. Formal analysis: H.L., C.D. and J.D.

Writing—original draft: H.L. and C.D. Writing—review and editing: H.L., C.D. and J.D. Supversion: J.D. Funding acquistion: J.D. and C.D.

Competing interests

The authors declare no competing interests.

Additional information

Extended data is available for this paper at https://doi.org/10.1038/s41550-024-02347-z.

Supplementary information The online version contains supplementary material available at https://doi.org/10.1038/s41550-024-02347-z.

Correspondence and requests for materials should be addressed to Haiyang Luo, Caroline Dorn or Jie Deng.

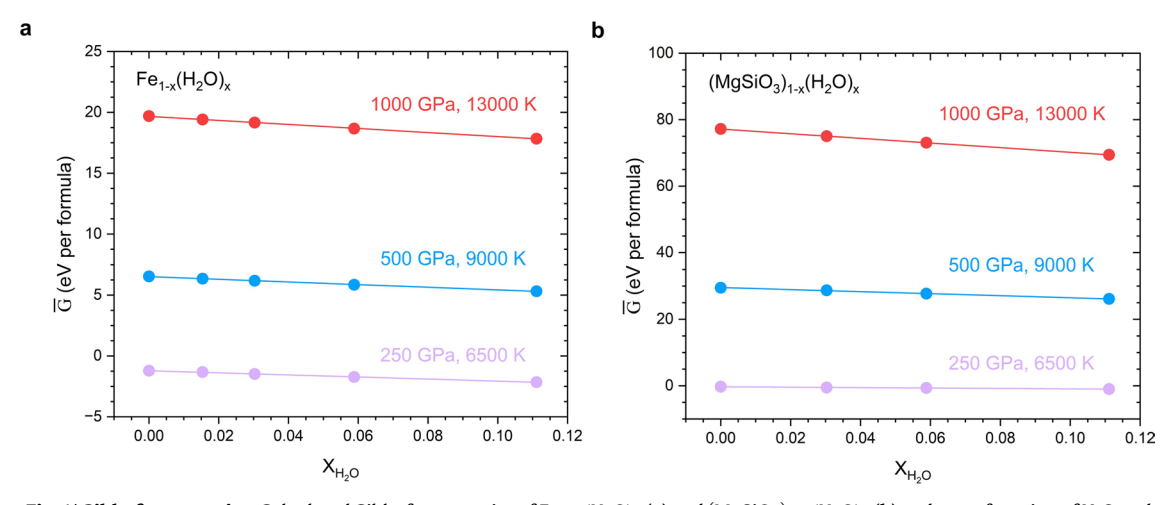
Peer review information *Nature Astronomy* thanks the anonymous reviewers for their contribution to the peer review of this work.

Reprints and permissions information is available at www.nature.com/reprints.

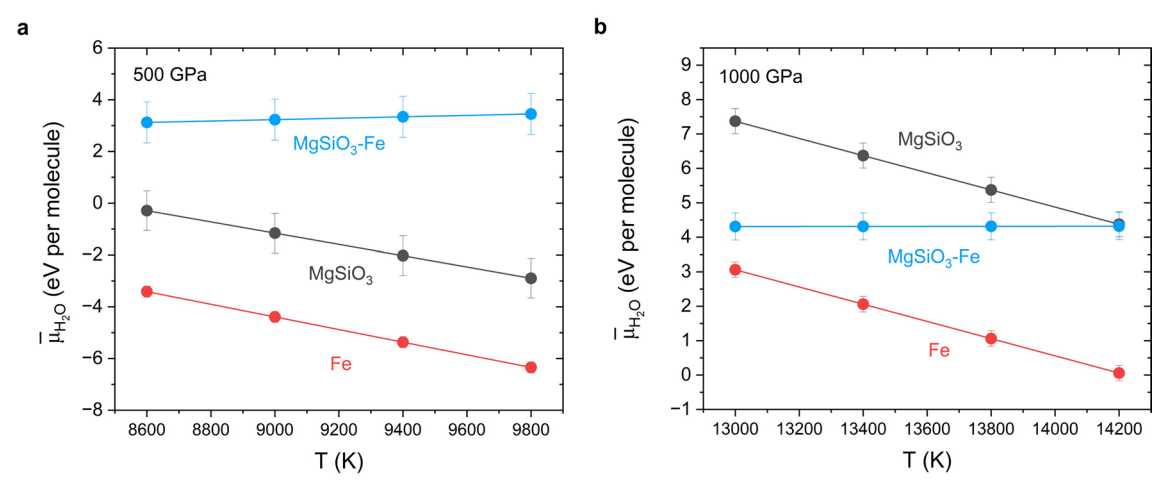
Publisher's note Springer Nature remains neutral with regard to jurisdictional claims in published maps and institutional affiliations.

Springer Nature or its licensor (e.g. a society or other partner) holds exclusive rights to this article under a publishing agreement with the author(s) or other rightsholder(s); author self-archiving of the accepted manuscript version of this article is solely governed by the terms of such publishing agreement and applicable law.

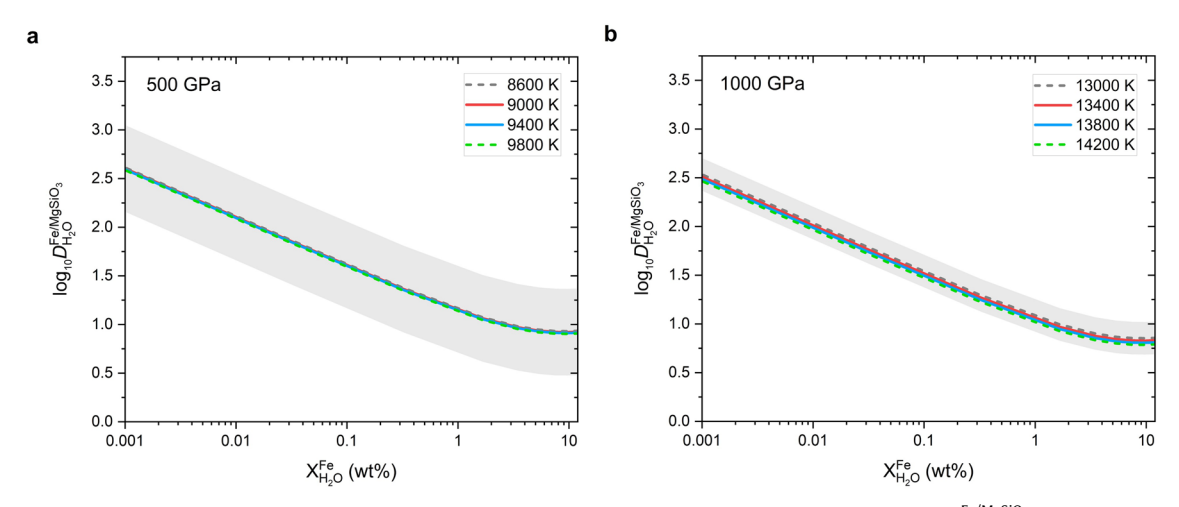
@ The Author(s), under exclusive licence to Springer Nature Limited 2024



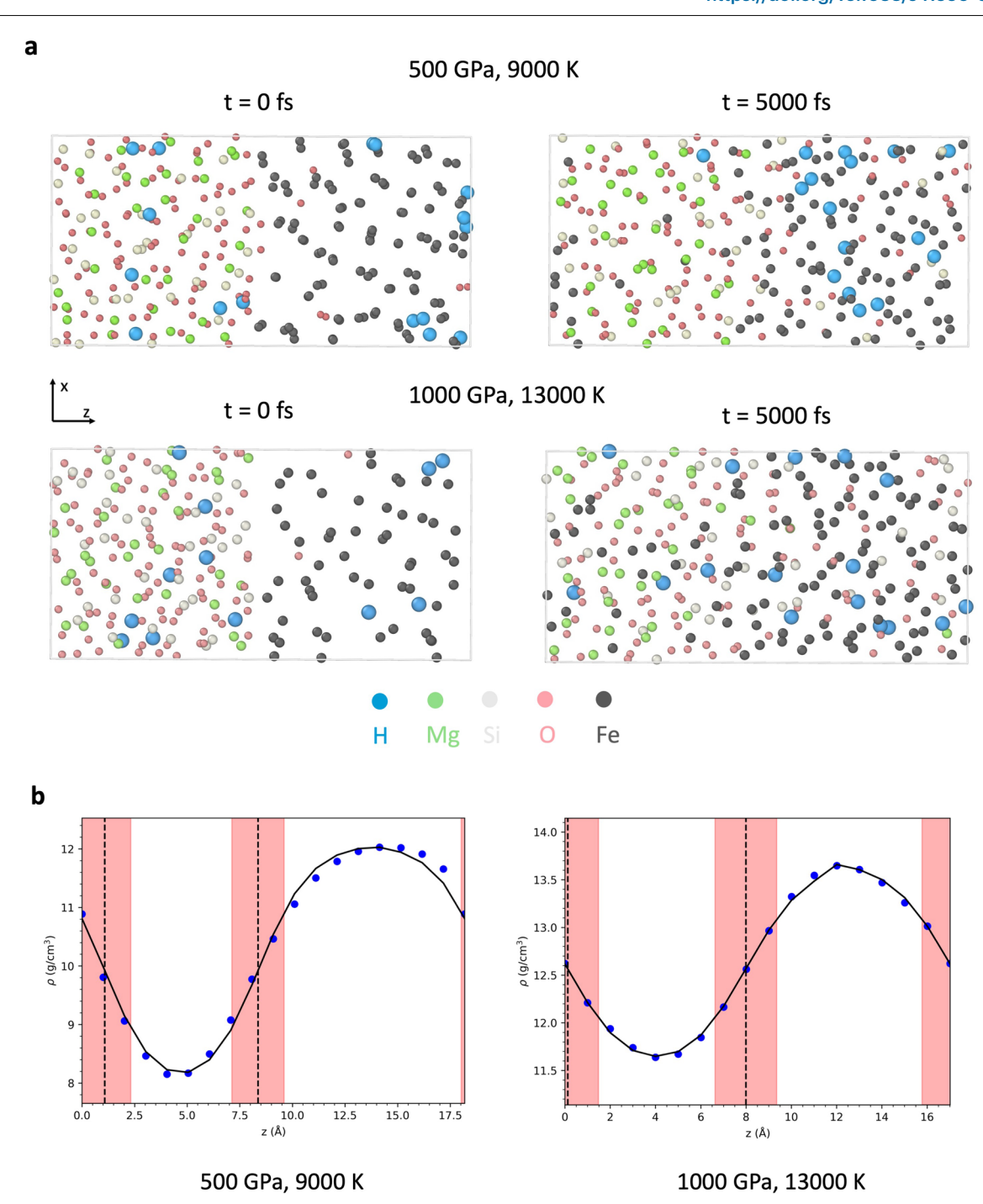
Extended Data Fig. 1 | **Gibbs free energies.** Calculated Gibbs free energies of $Fe_{1-x}(H_2O)_x$ (a) and $(MgSiO_3)_{1-x}(H_2O)_x$ (b) melts as a function of H_2O mole fractions (X_{H_2O}).



Extended Data Fig. 2 | **Chemical potentials of H_2O.** Calculated chemical potentials of H_2O in iron (Fe) and silicate (MgSiO₃) melts and their differences (MgSiO₃-Fe) at different temperatures under 500 GPa (a) and 1000 GPa (b). The 1 s.d. uncertainties of chemical potentials are shown. Lines connecting the data points are shown for clarity.

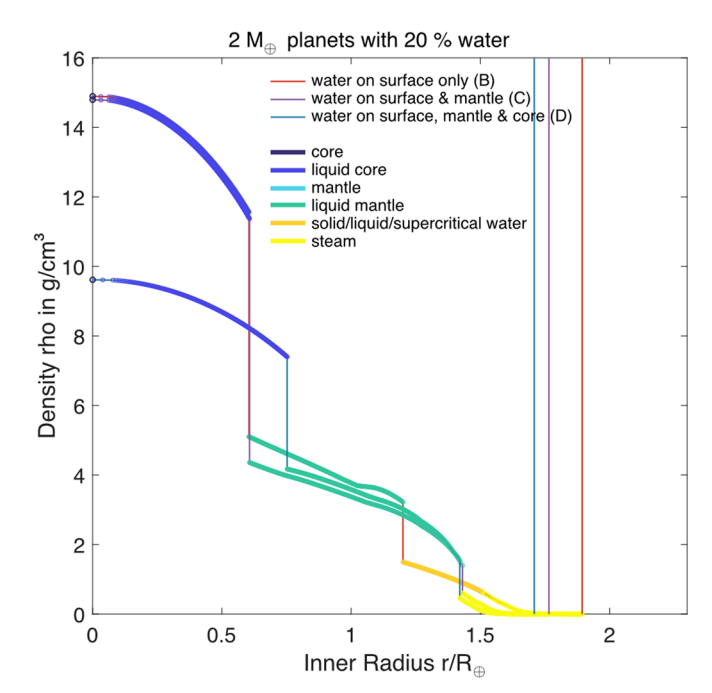


Extended Data Fig. 3 | Partition coefficients of H_2O . Calculated partition coefficients of H_2O between iron and silicate melts ($D_{H_2O}^{Fe/MgSiO_3}$) as a function of its concentrations in iron melt ($X_{H_2O}^{Fe}$) at different temperatures under 500 GPa (a) and 1000 GPa (b). The 1 s.d. uncertainties of $D_{H_2O}^{Fe/MgSiO_3}$ at 8600 and 13000 K are represented by the shaded area.



Extended Data Fig. 4 | **Molecular dynamics simulations of water partitioning.** Two-phase coexistence simulations of water ($X_{\rm H_{2O}}=1.54~\rm kt\%$) partitioning between iron (Fe) and silicate (MgSiO₃) melts at 500 GPa/9000 K and 1000 GPa/14000 K. **a**, The initial configurations and the snapshots at

5000 femtoseconds (fs) are shown. **b**, The corresponding instantaneous coarse-grained density profile (filled circles) along the z-axis of the simulation box at 5000 fs and the best fitting curve (solid line). The dashed vertical lines represent the locations of Gibbs dividing surfaces.



Extended Data Fig. 5 | Density profiles for planets of 2 $\,M_{\oplus}$ and 20 % bulk water mass fraction at T_{eq} of 700 $\,$ K. The total radius for each of the scenarios is highlighted as a vertical line (red: B, lilac: C, blue: D). The different distributions of water in planets change density structure, thermal structure (not shown),

melting temperatures (not shown), and hence the extent of molten layers. Wherever the density profiles seem to flatten, we checked that all densities increase at all pressures. The density difference at the core-mantle boundary here is larger than that shown in the Extended Data Fig. 4b due to pressure differences.

Extended Data Table 1 | Calculated Gibbs free energies

\overline{P}	T	System	V	$ar{G}$	System	V	$ar{G}$
(GPa)	(K)		(Å ³ /atom)	(eV/atom)		(Å ³ /atom)	(eV/atom)
50	3500	Fe ₆₄	9.722	-8.289 ± 0.005	(MgSiO ₃) ₃₂	8.072	-6.058 ± 0.003
250	6500		7.544	-1.215 ± 0.007		5.694	-0.058 ± 0.006
500	9000		6.434	6.538 ± 0.012		4.696	5.905±0.007
1000	13000		5.353	19.691±0.017		3.780	15.440±0.008
50	3500	Fe ₆₄ (H ₂ O) ₁	9.467	-8.133 ± 0.004	(MgSiO ₃) ₃₂ (H ₂ O) ₁	8.033	-6.022 ± 0.003
250	6500		7.314	-1.288 ± 0.010		5.641	-0.107 ± 0.006
500	9000		6.232	6.160 ± 0.014		4.646	5.815 ± 0.008
1000	13000		5.189	18.836±0.016		3.744	15.189±0.008
50	3500	Fe ₆₄ (H ₂ O) ₂	9.232	-7.983 ± 0.004	(MgSiO ₃) ₃₂ (H ₂ O) ₂	7.985	-5.993 ± 0.004
250	6500		7.108	-1.403 ± 0.008		5.593	-0.137 ± 0.005
500	9000		6.057	5.831±0.014		4.604	5.681 ± 0.008
1000	13000		5.035	18.060±0.016		3.709	14.964±0.008
50	3500	Fe ₆₄ (H ₂ O) ₄	9.722	-7.716 ± 0.003	(MgSiO ₃) ₃₂ (H ₂ O) ₄	7.898	-5.945 ± 0.003
250	6500		6.754	-1.548 ± 0.007		5.491	-0.211 ± 0.006
500	9000		5.738	5.237±0.010		4.522	5.472 ± 0.007
1000	13000		4.767	16.702 ± 0.014		3.642	14.531 ± 0.007
250	6500	Fe ₆₄ (H ₂ O) ₈	6.189	-1.765 ± 0.007			
500	9000		5.239	4.352±0.008			
1000	13000		4.342	14.594±0.011			

Simulations were conducted at 50, 250, 500, and 1000 GPa, corresponding to temperatures of 3500, 6500, 9000, and 13000 K, respectively.

$\textbf{Extended Data Table 2} \ | \ \textbf{Calculated Gibbs free energies as a function of temperature at 500 and 1000 GPa}$

P	T	System	V	$ar{G}$	System	V	$ar{G}$
(GPa)	(K)		(Å ³ /atom)	(eV/atom)		(ų/atom)	(eV/atom)
500	8600	Fe ₆₄	6.407	7.019	(MgSiO ₃) ₃₂	4.670	6.236
	9000		6.434	6.538		4.696	5.905
	9400		6.452	6.039		4.711	5.565
	9800		6.465	5.537		4.736	5.216
500	8600	Fe ₆₄ (H ₂ O) ₄	5.719	5.689	(MgSiO ₃) ₃₂ (H ₂ O) ₂	4.582	6.012
	9000		5.738	5.237		4.604	5.681
	9400		5.762	4.762		4.622	5.343
	9800		5.776	4.287		4.643	4.998
1000	13000	Fe ₆₄	5.353	19.691	(MgSiO ₃) ₃₂	3.780	15.437
	13400		5.366	19.160		3.791	15.069
	13800		5.378	18.636		3.803	14.695
	14200		5.387	18.105		3.811	14.317
1000	13000	Fe ₆₄ (H ₂ O) ₄	4.767	16.702	(MgSiO ₃) ₃₂ (H ₂ O) ₂	3.709	14.964
	13400		4.778	16.218		3.719	14.599
	13800		4.786	15.723		3.726	14.227
	14200		4.796	15.224		3.737	13.849

The temperature ranges from 8600 to 9800 K at 500 GPa, and from 13000 to 14200 K at 1000 GPa.